AFRL-RV-HA-TR-2008-1029

Spectral Studies of Shallow Earthquakes and Explosions: Implications for P/S Energy Partitioning, Stress Drop, and Discrimination

Peter Shearer
Bettina Allmann

Institute of Geophysics and Planetary Physics
Scripps Institution of Oceanography
University of California, San Diego
8800 Biological Grade
La Jolla, CA 92093-0225

Final Report

16 January 2008

APPROVED FOR PUBLIC RELEASE; DISTRIBUTION UNLIMITED.

AIR FORCE RESEARCH LABORATORY
Space Vehicles Directorate
29 Randolph Road
AIR FORCE MATERIEL COMMAND
Hanscom AFB, MA 01731-3010

NOTICE AND SIGNATURE PAGE

AFRL-RV-HA-TR-2008-1029 HAS BEEN REVIEWED AND IS APPROVED FOR PUBLICATION IN ACCORDANCE WITH ASSIGNED DISTRIBUTION STATEMENT.

//Signature//	//Signature//
ROBERT RAISTRICK Contract Manager	PAUL TRACY, Acting Chief Battlespace Surveillance Innovation Center

REPORT DOCUMENTATION PAGE [example]

Form Approved
OMB No. 0704-0188

1. REPORT DATE 17 Dec 2007

2. REPORT TYPE Final Report

3. DATES COVERED *(From - To)* 17 Dec 2005 to 17 Dec 2007

4. TITLE AND SUBTITLE
Spectral Studies of Shallow Earthquakes and Explosions: Implications for P/S Energy Partitioning, Stress Drop, and Discrimination

5a. CONTRACT NUMBER FA8718-06-C-0004

5b. GRANT NUMBER N/A

5c. PROGRAM ELEMENT NUMBER 62601F

5d. PROJECT NUMBER 1010

5e. TASK NUMBER SM

5f. WORK UNIT NUMBER A1

6. AUTHOR(S)
P. Shearer and B. Allmann

7. PERFORMING ORGANIZATION NAME(S) AND ADDRESS(ES)
IGPP/SIO
U.C. San Diego
La Jolla, CA 92093-0225

8. PERFORMING ORGANIZATION REPORT NUMBER

9. SPONSORING / MONITORING AGENCY NAME(S) AND ADDRESS(ES)
Air Force Research Laboratory
29 Randolph Rd.
Hanscom AFB, MA 01731-3010

10. SPONSOR/MONITOR'S ACRONYM(S) AFRL/RVBYE

11. SPONSOR/MONITOR'S REPORT NUMBER(S) AFRL-RV-HA-TR-2008-1029

12. DISTRIBUTION / AVAILABILITY STATEMENT
Approved for Public Release; Distribution Unlimited.

13. SUPPLEMENTARY NOTES

14. ABSTRACT
We compute and analyze *P*-wave spectra from 18,101 earthquakes and 1770 explosions recorded by 196 broadband seismic stations in southern California at epicentral distances up to 100 km. We use an online waveform database stored on a RAID system at Caltech, which provides complete access to the Southern California Seismic Network (SCSN) seismogram archive. We compute spectra using 1.28 s noise and signal windows, positioned immediately before and after the *P* arrivals. After applying a signal-to-noise cutoff, we process the spectra using an iterative robust least-squares method to isolate source, receiver, and propagation path contributions. This corrects for first-order attenuation structure, as well as near-receiver site effects and any errors in the instrument response functions. Using the earthquake spectra and a simple source model, we compute an empirical Green's function to remove the tradeoff between the source terms and other terms in our model. Our observed earthquake spectra are fit reasonably well with a constant stress drop model over a wide range of moment. However, the explosion spectra show significant differences from the earthquake spectra and have generally steeper falloffs at high frequencies. We also compare *P* and *S*-wave amplitudes and find modestly smaller average *S* amplitudes for the explosions compared to the earthquakes. The best earthquake/explosion discriminant is the RMS misfit to an ω^{-2} source model, which works for ~90% of the events.

15. SUBJECT TERMS
Spectral analysis, Seismic discrimination

16. SECURITY CLASSIFICATION OF:			17. LIMITATION OF ABSTRACT	18. NUMBER OF PAGES	19a. NAME OF RESPONSIBLE PERSON
a. REPORT	**b. ABSTRACT**	**c. THIS PAGE**			Robert Raistrick
UNCLASSIFIED	UNCLASSIFIED	UNCLASSIFIED	SAR	33	**19b. TELEPHONE NUMBER** *(include area code)* 781-377-3726

Table of Contents

Figures

1. SUMMARY

Routine seismic discrimination between earthquakes and explosions has been a long-standing goal in nuclear test ban treaty research (for a recent review, see Stump et al., 2002). A variety of methods have been employed, including amplitude ratios among regional phases (e.g., Bennett and Murphy, 1986; Wuster, 1993; Plafcan et al., 1997; McLaughlin et al., 2004), spectral studies (e.g., Taylor et al., 1988; Gitterman and van Eck, 1993; Kim et al., 1994; Walter et al., 1995; Gitterman et al., 1998), coda studies (e.g., Su et al., 1991; Hartse et al., 1995), ripple-fire detection schemes (e.g., Hedlin et al., 1990; Smith, 1993; Carr and Garbin, 1998; Hedlin, 1998; Arrowsmith et al., 2006), and other methods (e.g., Musil and Plesinger, 1996; Parolai et al., 2002; Leidig et al., 2004; Tibuleac et al., 2004).

The goal of this project is to systematically analyze and compare source spectra from locally recorded earthquakes and explosions in southern California (Figure 1) in order to develop new insights into discrimination methods. Advances in data storage and computer capabilities make possible much more extensive analyses than have been performed in the past, which will provide a better picture of the distribution of source spectral properties and amplitudes. By examining tens of thousands of events, we will quantitatively characterize differences between earthquakes and explosions in terms of their spectral content and their *P/S* energy ratios. We also plan to identify and examine anomalous events, in particular earthquakes that may appear like explosions in spectral discrimination methods in order to determine how common they are and whether alternate discrimination techniques can be applied.

The project builds upon a recently completed large-scale analysis of southern California earthquake spectra (Shearer et al., 2006), to include a set of 1770 mining and other explosions between 2000 and 2005. The Shearer et al. earthquake study has already provided the largest set of earthquake spectra and stress drops computed to date, showing that individual event stress drops range between 0.2 and 20 MPa. The large number of stations and events available in southern California make possible empirical calibration methods to remove receiver response and path propagation effects. Our efforts focus on southern California because of the unmatched size and quality of the available data, but we expect the results and insights will be applicable to other regions of more direct interest to nuclear monitoring programs. While the Shearer et al. (2006) study analyzed 1989–2001 data from short-period vertical-component stations, we examine 2000–2005 data from three-component, broadband stations. The newer data have the advantage of the horizontal components and a larger dynamic range (i.e., the older data clip on earthquakes above ~M3.5).

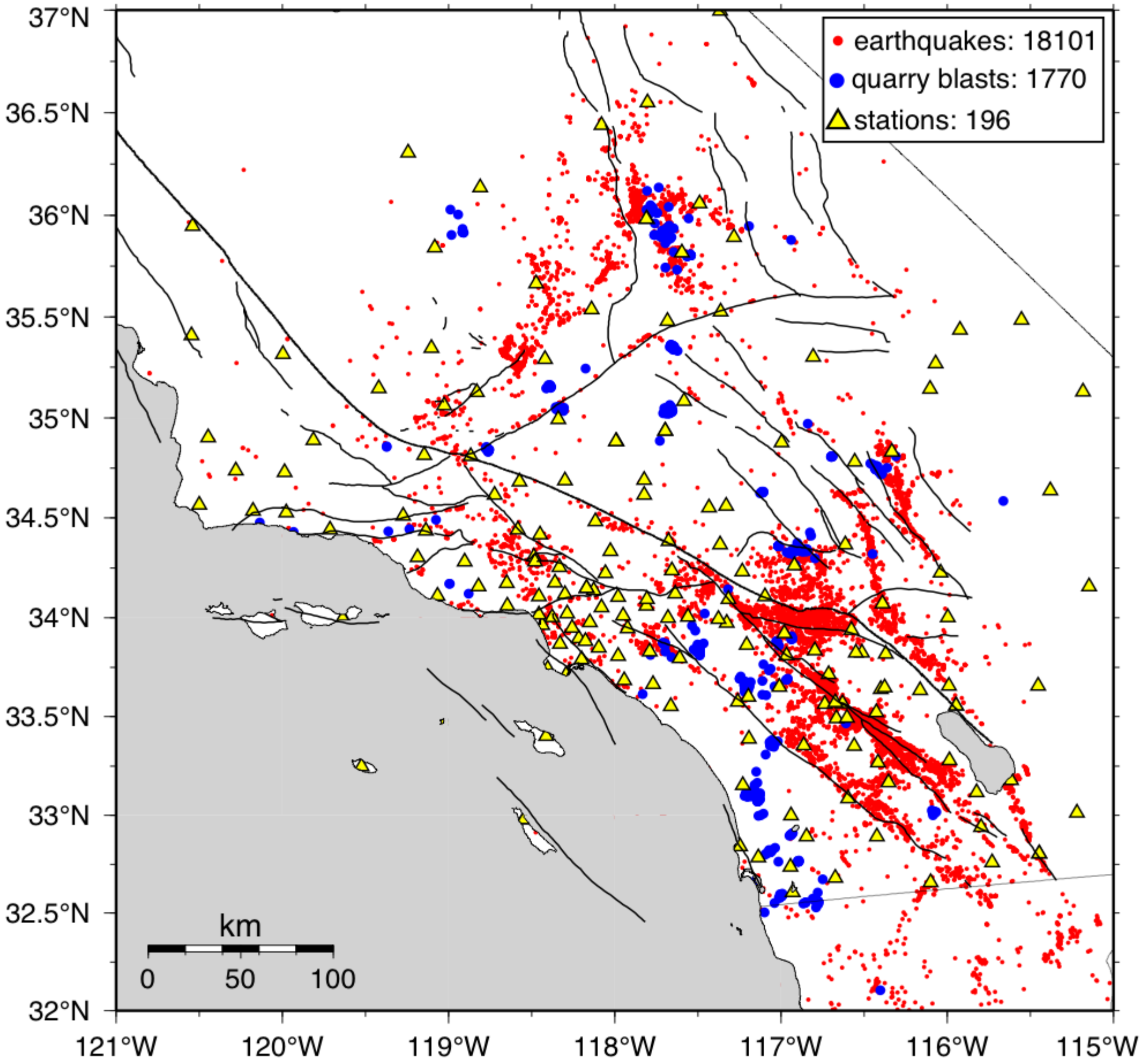

Figure 1. Locations of 18,101 earthquakes (red) and 1770 explosions (blue) in southern California from 2000 to 2005 as recorded by broadband stations (yellow) of the Southern California Seismic Network (SCSN).

2. TECHNICAL APPROACH

The Southern California Seismic Network (SCSN) has several hundred stations and records about 12,000 to 35,000 earthquakes each year. Recently we began storing seismograms from all archived events in an online RAID system that provides rapid and random access to the data (Hauksson and Shearer, 2005). Spectra are computed as follows: For each seismogram we pick the *P* and *S* arrivals and estimate their amplitudes. This is done using the operator pick, if available, or using the output of an automatic picking algorithm for a window around the predicted arrival time (based on the catalog event location and a 1-D velocity model). Traces are resampled to a uniform 100 Hz sample rate. Spectra are computed for 1.28 s noise and signal windows, immediately before and after the pick time. We compute results for all available channels and components for both *P* and *S*, including rotation of the horizontals (if present) into transverse and radial records. Both signal and pre-event noise spectra are corrected to displacement and stored in a special binary format.

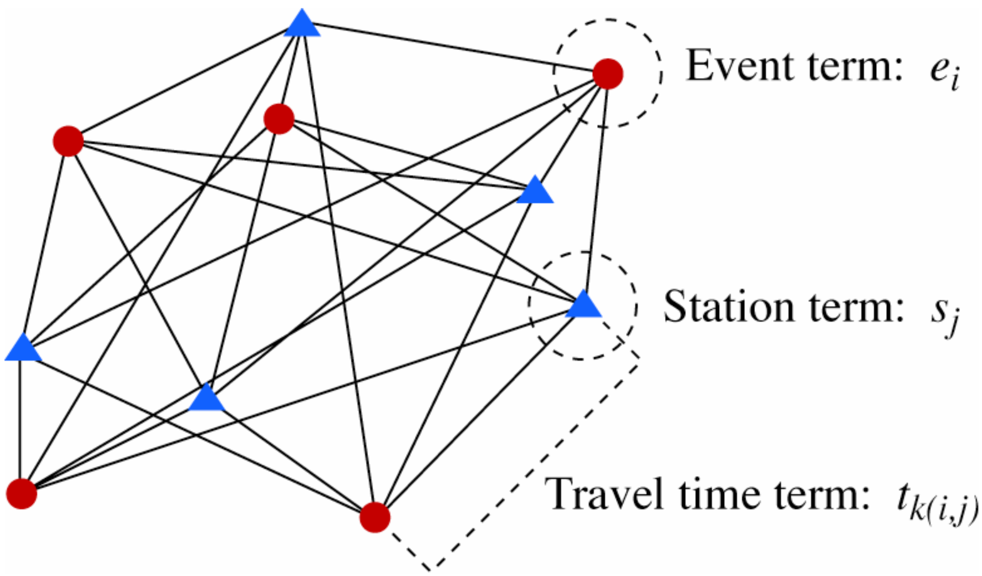

Figure 2. A cartoon showing how measured spectra can be modeled as a product of event, station, and travel-time dependent terms.

We apply a signal-to-noise (STN) cutoff to the spectra, requiring that the STN amplitude ratio be at least 5 for three separate bands of 5 to 10 Hz, 10 to 15 Hz and 15 to 20 Hz. Next, we process the spectra in order to isolate source, receiver and propagation path effects. This is an important step because individual spectra tend to be irregular in shape and difficult to fit robustly with theoretical models. However, by stacking and analyzing thousands of spectra it is possible to obtain more consistent results. The basic approach is illustrated in Figure 2 and is similar to that used by Warren and Shearer (2000, 2002) and Prieto et al. (2004). Each observed displacement spectrum $d_{ij}(f)$ from source *i* and receiver *j* is a product of a source term e_i (which includes the source spectrum and near-source attenuation), a near-receiver term s_j (which includes any uncorrected part of the instrument response, the site response and the near-receiver attenuation), and a travel-time dependent term $t_{k(i,j)}$ (which includes the effects of geometrical spreading and attenuation along the ray path). In the log domain, this product becomes a sum:

$$d_{ij} = e_i + s_j + t_{k(i,j)} + r_{ij}$$

where r_{ij} is the residual for path *ij*. We parameterize *t* in terms of the predicted *P* travel time between the source and receiver, using the event locations and velocity model from Lin et al. (2007). This accounts for both the event depth and the source-receiver distance.

The travel-time term $t_{k(i,j)}$ is discretized by its index k at 1 s increments in travel time. Because each station records multiple events and each event is recorded by multiple stations, this is an over-determined problem. We solve this equation using a robust, iterative, least-squares method in which we sequentially solve individually for the terms t_k, s_j, and e_i, keeping the other terms fixed at each stage. We suppress outliers by assigning L1-norm weights to misfit residuals greater than 0.2 s (or less than -0.2 s). This weighting scheme is necessary to ensure robustness with respect to a small number of spectra with large excursions compared to the bulk of the data. In practice we found that the method converged rapidly to a stable solution after a few iterations.

Radiation pattern differences are not included and would be difficult to include in our processing because they are not generally available for the smaller magnitude events. By using multiple stations for each source, however, radiation pattern effects will tend to average out. Note that this method resolves only differences in the relative shapes of the spectra. Without additional modeling assumptions, it cannot, for example, resolve how much of the spectral falloff is due to source effects and how much is due to attenuation common to all paths. The advantage of the method, however, is that it identifies and removes anomalies that are specific to certain sources or receivers. Because there may be difficulties in obtaining reliable and accurate instrument response functions for many of the stations in the archive, this is an important processing step that provides a way to correct for some of these problems.

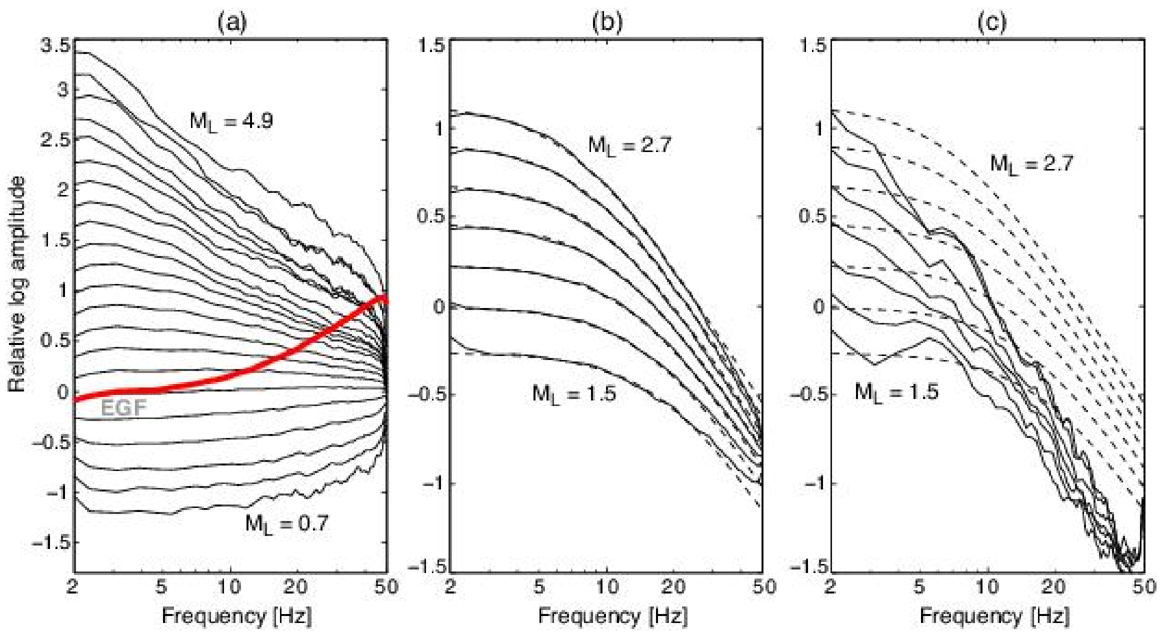

Figure 3. Stacked P-wave source displacement spectra from 2000 to 2005 within bins of estimated seismic moment for 17810 earthquakes and 1744 quarry blasts. (A) Stacked earthquake source terms obtained from the iterative inversion. Red line shows the empirical Green's function (EGF) used to correct these spectra for attenuation and other path effects assuming a constant stress drop model. (B) EGF corrected earthquake source terms compared to predictions of the Madariaga (1976) source model (dashed lines). (C) Stacked source terms for quarries.

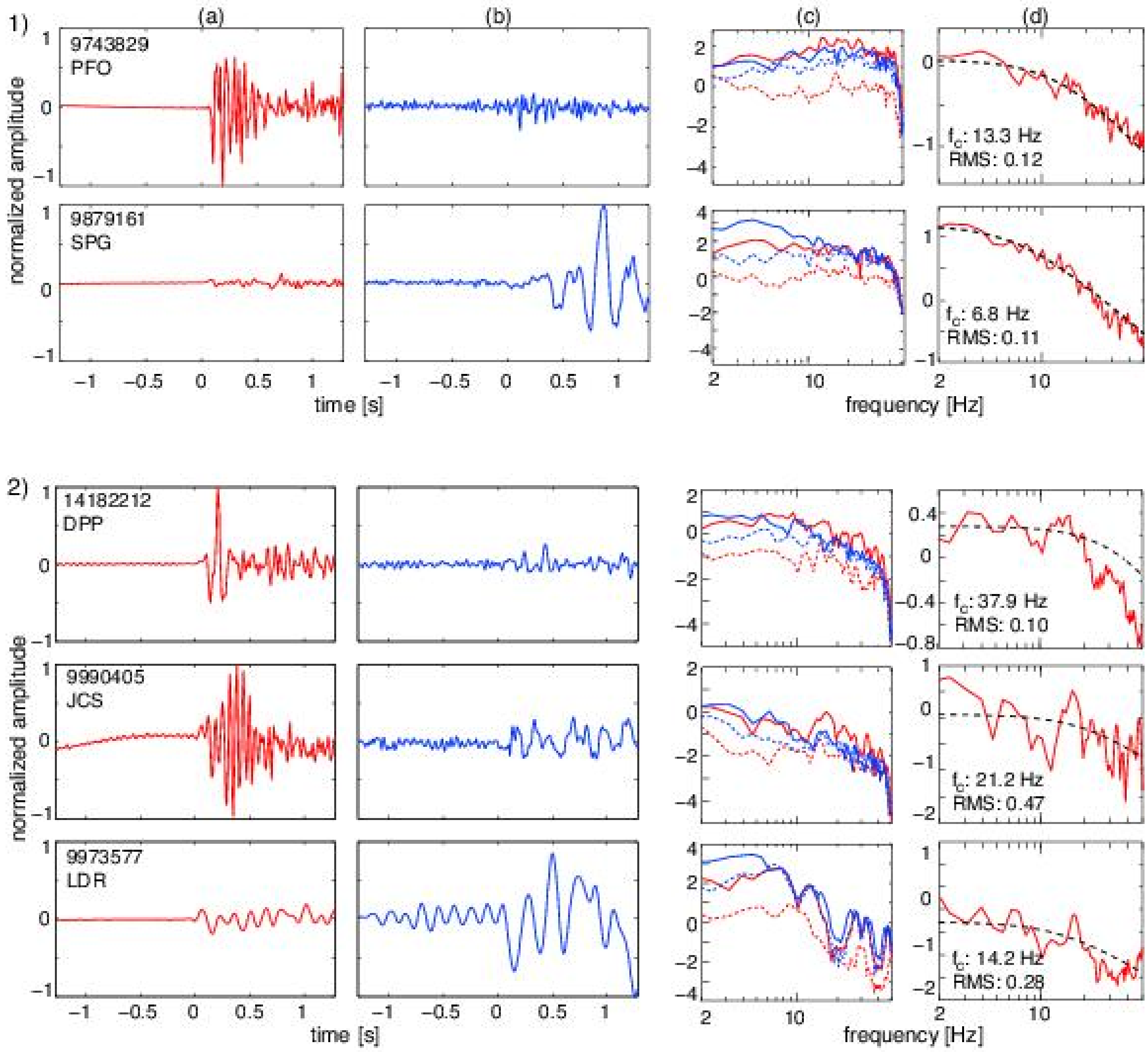

Figure 4. (1) Two examples of earthquake waveforms and spectra. (2) Three examples of quarry blast waveforms and spectra. (a) Waveforms windowed around the P-wave first arrival recorded on the vertical component. Event ID and station acronym are shown in the upper left. (b) Waveforms windowed around the S-wave arrival recorded on the rotated transverse component of same station. (c) Spectra for P (solid red), S (solid blue), and respective noise levels (dashed red and dashed blue). (d) EGF-corrected P-wave source spectra (red) together with the best-fitting source model (dashed).

3. RESULTS AND DISCUSSION

Our focus has been on the stacked source spectra, e_i, which we ultimately use to estimate the moment and corner frequency of each event. At this stage, however, the source spectra only contain relative information among the different events. In order to estimate absolute spectra from our source stacks, we use the local magnitude M_L to obtain the scaling factor necessary to convert our relative moment estimates to absolute moment and we use an empirical Green's function approach to correct the spectral shapes for attenuation and other path effects (for details, see Shearer et al., 2006). To study the average shape of the spectra, we stack our results within equally spaced bins in estimated seismic moment (obtained from the low-frequency part of the spectrum). Figure 3 shows these stacked spectra for both earthquakes and quarry blasts. The dashed lines show the best-fitting predictions of the ω^{-2} source model of Madariaga (1976), assuming a constant stress drop.

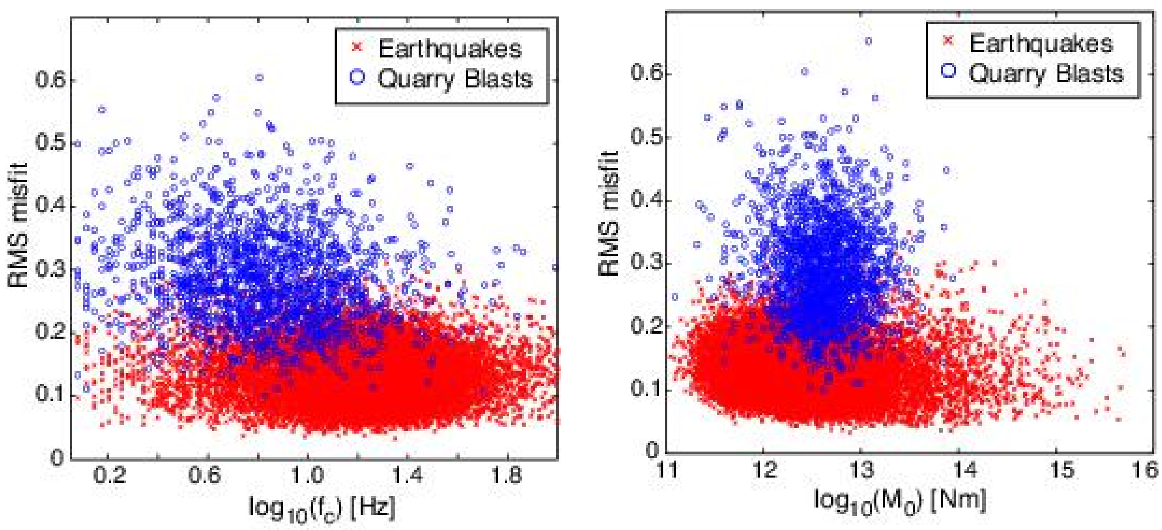

Figure 5. Left: RMS Misfit vs. corner frequency for earthquakes (red) and quarry blasts (blue). Right: RMS misfit vs. seismic moment.

Figure 3 shows that averaged earthquake spectra in southern California are well fit by a standard source model. However, the averaged quarry spectra appear anomalous in at least two respects: (1) They exhibit large misfit compared to the source model predictions, and (2) They have generally steeper falloffs at high frequencies than ω^{-2}, which will lead to lower corner frequencies and stress drop estimates. The lack of high frequency radiation from the quarries is somewhat surprising and may reflect ripple firing and/or strong near-surface attenuation. The effect is also apparent in individual source spectra, as illustrated in Figure 4. Here, we show example waveforms and spectra for earthquakes and events labeled as quarry blasts, at good and fair signal-to-noise ratios. The spectra for the two earthquakes fit the theoretical source spectra much better than the quarry blast spectra. We also notice that the signal-to-noise ratio is fairly poor for most S-wave spectra. We attribute this to contamination from P coda. We have therefore focused our study on the P-wave spectra obtained from vertical components.

In any case, we attempt to use these two differences to discriminate between earthquakes and quarry blasts in southern California. We do this by computing the best-fitting ω^{-2}

source model to the individual EGF-corrected source spectra. For each event, we obtain an estimate of the moment, the corner frequency and a measure of the RMS misfit to the source model. Figure 5 shows the spectral misfit plotted against the corner frequency and the seismic moment. First of all, we notice that the spectral misfit does not depend on either the corner frequency of the spectrum or the seismic moment of the event, which makes this parameter viable to be used as a discriminant. Note that the quarry blasts have generally higher misfits and smaller corner frequencies than the explosions. We also observe that earthquakes span a much wider moment range than the man-made explosions. In general, the two populations are not completely separated and there is some degree of overlap, particularly in the corner frequency estimates. Figure 6 shows the separation of the two populations in the corner frequency-moment domain, with lines of constant stress drop indicated. We obtain generally lower stress drop estimates for the quarry blasts, even though stress drop is not defined for an artificial explosion. We also observe that the distribution of earthquake stress drops implies self-similarity (stress drop not dependent on moment), although the scatter increases toward smaller moments.

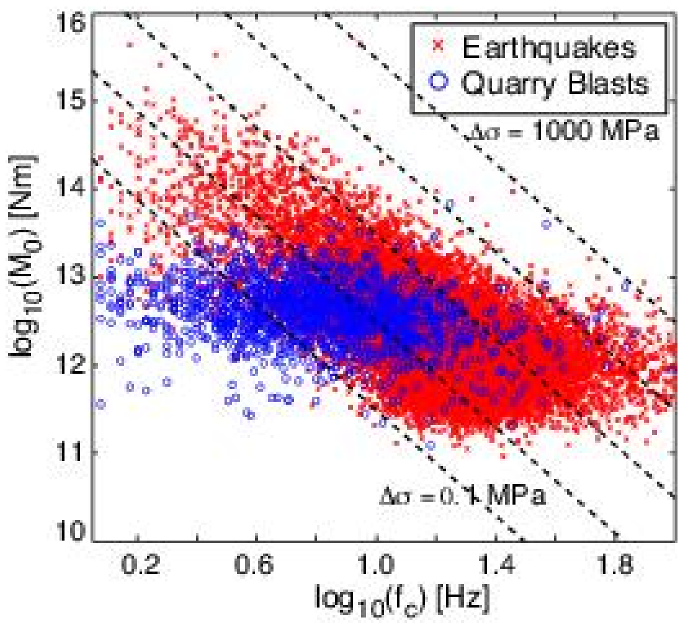

Figure 6. Moment vs. corner frequency of earthquakes (red) and quarry blasts (blue). The dashed lines represent stress drop estimates according to the Madariaga (1976) model.

We next look at histograms of the earthquake and quarry blast distributions with respect to RMS misfit (Fig. 7) to see how well the populations separate. We find an empirical value of 0.2 RMS misfit at which the earthquake and quarry blast populations separate at the 90% level. In other words, 90% of the earthquakes show an RMS misfit of < 0.2, whereas 90% of the quarry blasts show an RMS misfit of > 0.2, A similar histogram with respect to corner frequency (Fig. 8) shows an overall weaker separation, where the 10% and 90% quantile cannot be drawn at the same corner frequency value. In order to rule out the possibility that the lower corner frequency observed for quarry blasts is an effect of the increased attenuation in the shallow subsurface and thus attributable to event depth, we compare the distribution of corner frequencies with shallow earthquakes only (Fig. 8 b). We note that there is no significant difference in the corner frequency distribution if the earthquake population is limited to depths shallower than 5 km. This confirms that the lower corner frequencies observed for quarry blasts are a source-related effect rather than an effect of near-source attenuation.

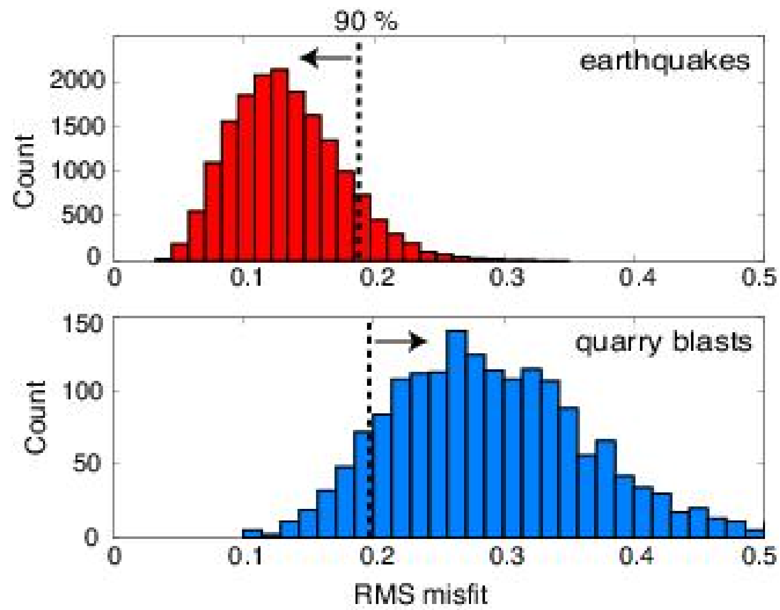

Figure 7. Histograms comparing the distribution of RMS misfit to an ω^{-2} source model for both earthquakes (top) and quarry blasts (bottom). The dashed vertical lines divide the distributions into 10% and 90% parts. Note that 90% of the quarries have model misfits greater than that of 90% of the earthquakes.

Our results from analysis of *S*-wave spectra from transverse-component records have so far been inconclusive, in part because of the generally lower signal-to-noise ratios at high frequencies for the *S* waves compared to the *P* waves. However, the amplitude ratio between *P*- and *S*-arrivals is an often-used discriminant for explosions. The idea here is that explosion sources preferentially excite compressional waves, whereas earthquakes are mainly due to shear on a fault, and thus radiate *S* waves in higher proportion.

In order to investigate whether the *S*/*P* ratio could be used as a discriminant in southern California, we pick the peak amplitudes of the *P*- and *S*-arrivals on seismograms with a signal-to-noise ratio of at least three for the *P* arrival. This analysis is conducted on seismograms that are filtered between 1 and 10 Hz. We obtain the *P* pick from the vertical component and the *S* pick from the rotated transverse component.

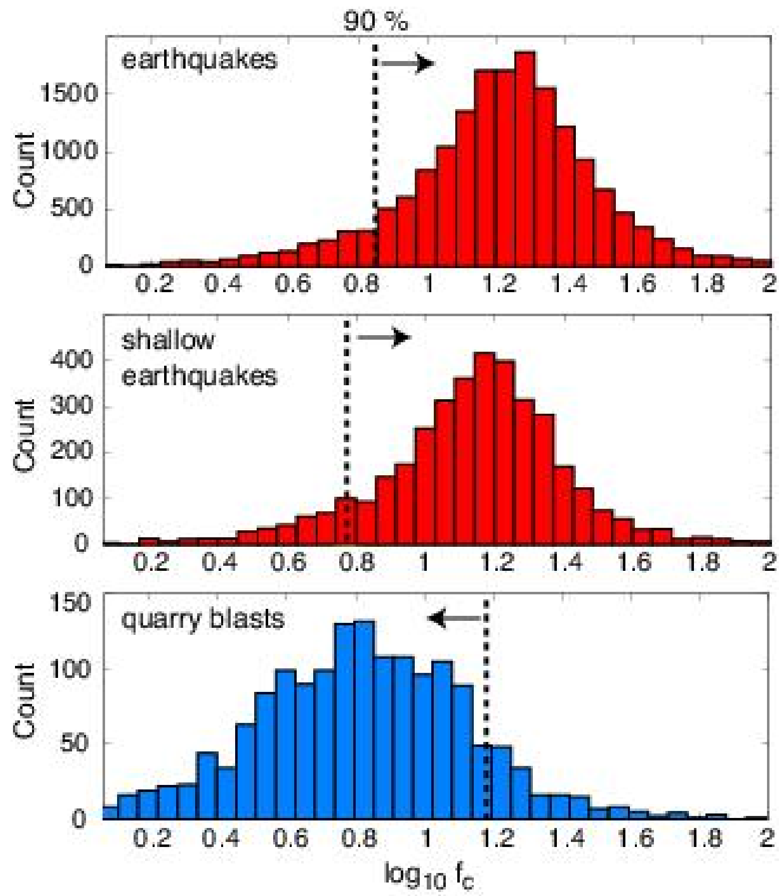

Figure 8: Histograms comparing the distribution of corner frequency for earthquakes (top), shallow earthquakes (middle) and quarry blasts (bottom). The dashed vertical lines divide the distributions into 10% and 90% parts.

Plotting the amplitude ratios as a histogram, separately for quarry blasts and natural earthquakes (Fig. 9), we observe slightly lower average *S/P* amplitude ratios for the quarries using simple peak amplitudes. However, the separation between the two populations is not apparent. We try to quantify the difference between the two populations by fitting a Gaussian distribution to the histogram, from which we obtain a mean and standard deviation for the *P/S* ratios of natural earthquakes and man-made explosions.

We observe that, for southern California, quarry blasts and earthquakes are not distinguishable by their *S/P* amplitude ratios. One reason for this could be the interference of *P* coda into the *S* arrivals. In order to avoid this possibility, we look at only records with an epicentral distance of greater than 100 km (see Fig. 10). This ensures that *P* and *S* arrivals are sufficiently separated in time in order that the *S* arrival is not contaminated by *P* coda. This amplitude ratio is comparable with a *Pn*/*Sn* ratio. We notice that the separation between the two populations is much more pronounced when we restrict the amplitude ratio analysis to epicentral distances greater than 100 km, roughly equivalent to the critical distance for the *Pn* phase. We observe that at these distances, the *S/P* ratios decrease for the quarry blasts, whereas they increase for the earthquakes. It should be noted, however, that restricting the epicentral distance to greater than 100 km could result in a bias because we are in effect restricting out database to look only at larger events. Overall, we notice that the *S/P* amplitude ratios are not very useful as a discriminant between earthquakes and explosions in southern California.

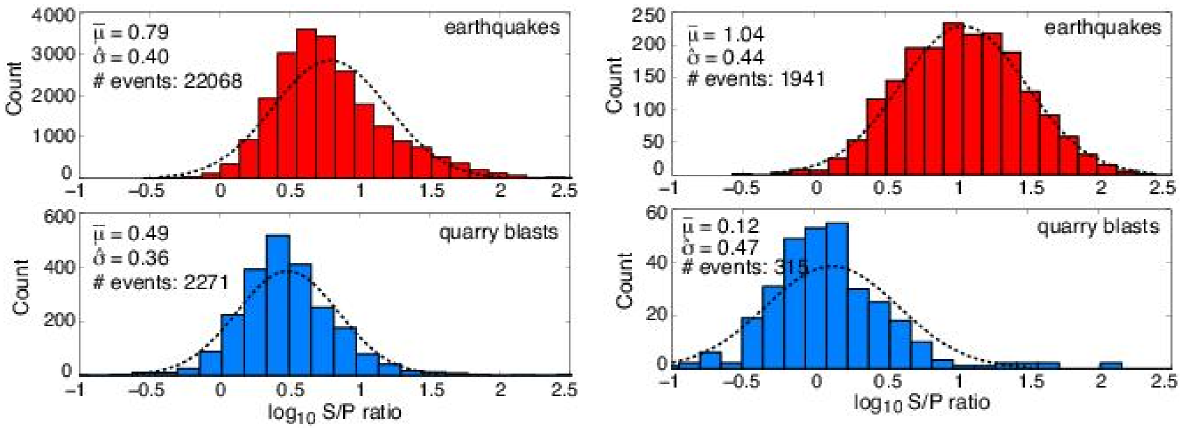

Figure 9. Histograms comparing the distributions of *S/P* amplitude ratios between earthquakes (top) and quarry blasts (bottom). The left panels include only traces with an epicentral distance of at least 100 km.

Next, we look at individual clusters of quarry blast events that can be attributed to individual operations. Most, but not all, of these locations can be attributed to mining. We look at 10 individual event clusters that are highlighted in Figure 10. Cluster 1 through 5, as well as cluster No. 8 are located in the Mojave Desert and can be correlated with surface mining operations visible in satellite imagery. Clusters 6,7 and 10 are located in densely populated areas of Riverside and San Diego County and cannot be easily correlated with a particular operation or surface feature. Some of these events may be due to grading and/or construction. Cluster No. 9 is more distributed in nature and covers the area of the China Lake Naval Air Weapons Station. We suspect that testing of military equipment could be adding to the catalog in this region. However, this is also an area with a high rate of natural seismicity, so it is likely that some events in this region may be mislabeled. Figures 11 to 20 represent summary plots for each individual cluster, showing the stacked spectra per magnitude bin, their respective fit to the standard source model, as well as histograms and cross plots for the misfit and the corner frequency. As before, we observe the generally steeper falloff rate of the spectra, leading to a high misfit with respect to an earthquake source model. These plots also help to identify possible characteristic patterns in a particular cluster. Such patterns could be indicative of particular blasting practices (i.e., ripple-fired explosions with characteristic delay times, surface vs. underground explosions, etc.). Such characteristic patterns are not directly evident from the plots. However, we do note slight differences between some of the clusters. For example, cluster 8 shows, on average, larger moment releases than, e.g., cluster 3. This could be an indication either of different charge sizes used in the two mining operations, or it could be related to the ground coupling (i.e., hard vs. soft rock).

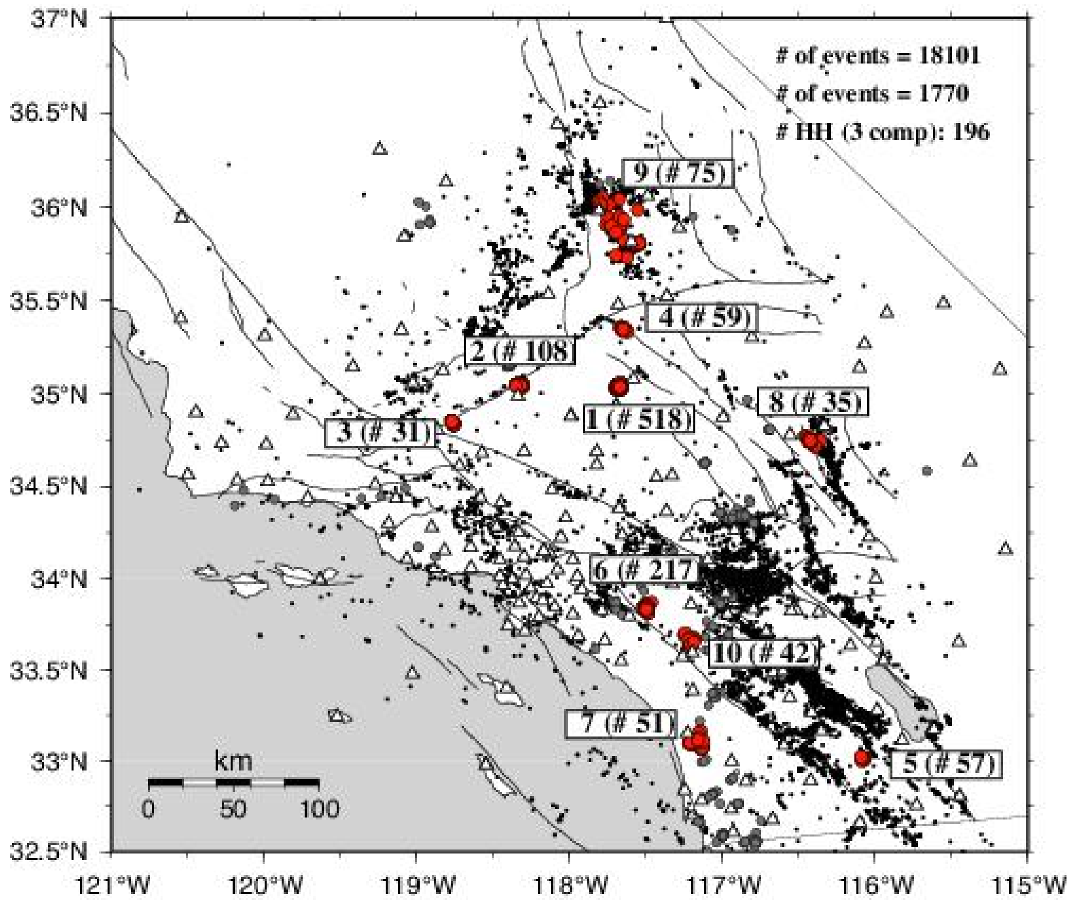

Figure 10. Locations of ten specific event clusters labeled as quarry blasts (red). Each cluster consists of a different number of individual events.

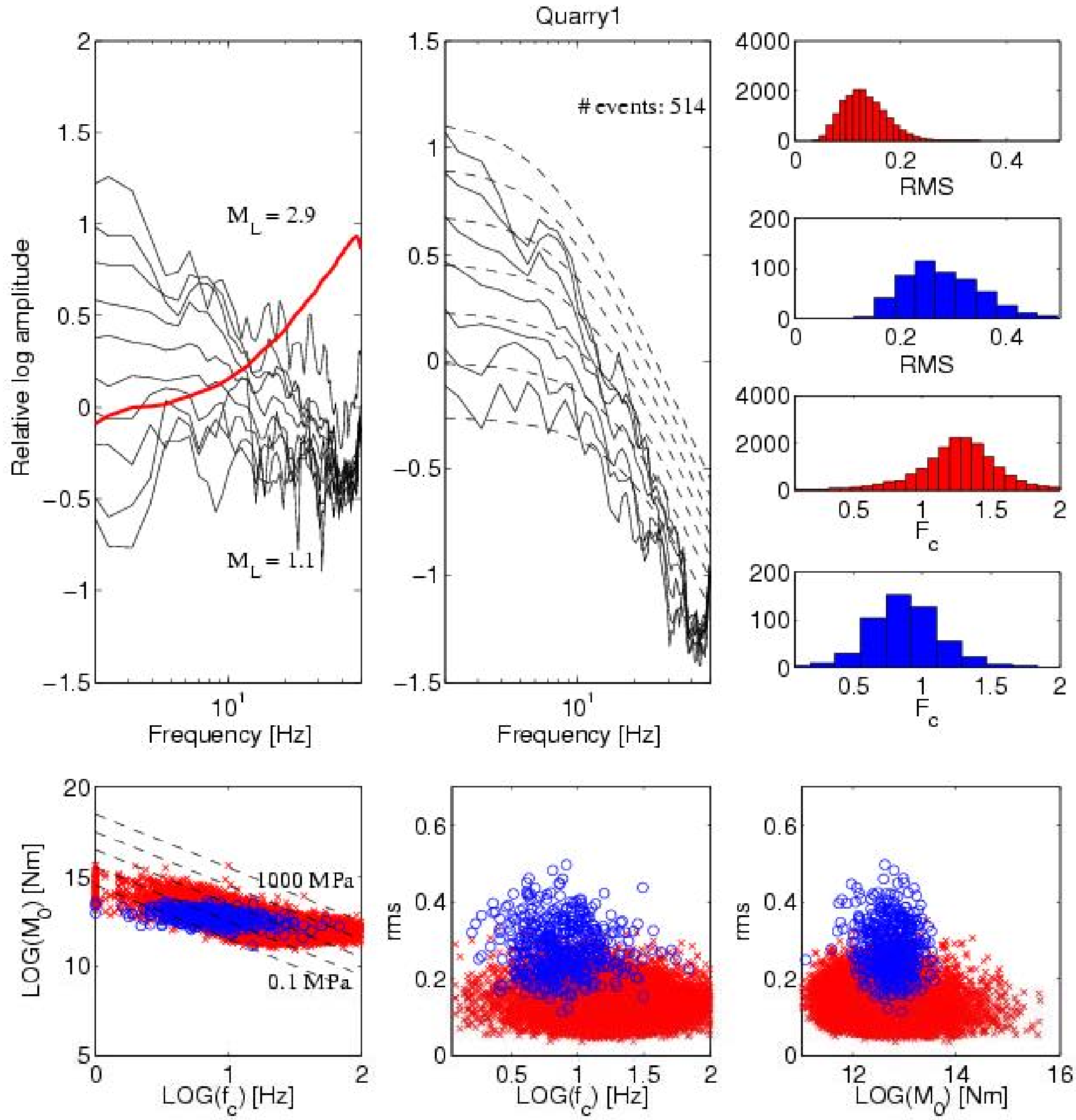

Figure 11. Example quarry 1 (see Fig. 10 for location). Upper left: Stacked quarry blast source spectra in 0.2 local magnitude bins. The red line shows the EGF computed from earthquake spectra. Upper middle: EGF corrected source spectra. Upper right: Histograms of rms-misfit and corner frequency for all earthquakes (red) and the quarry example (blue). The bottom panels from left to right show moment vs. corner frequency, rms-misfit vs. corner frequency, and rms-misfit vs. moment for all earthquakes (red) and the example quarry (blue).

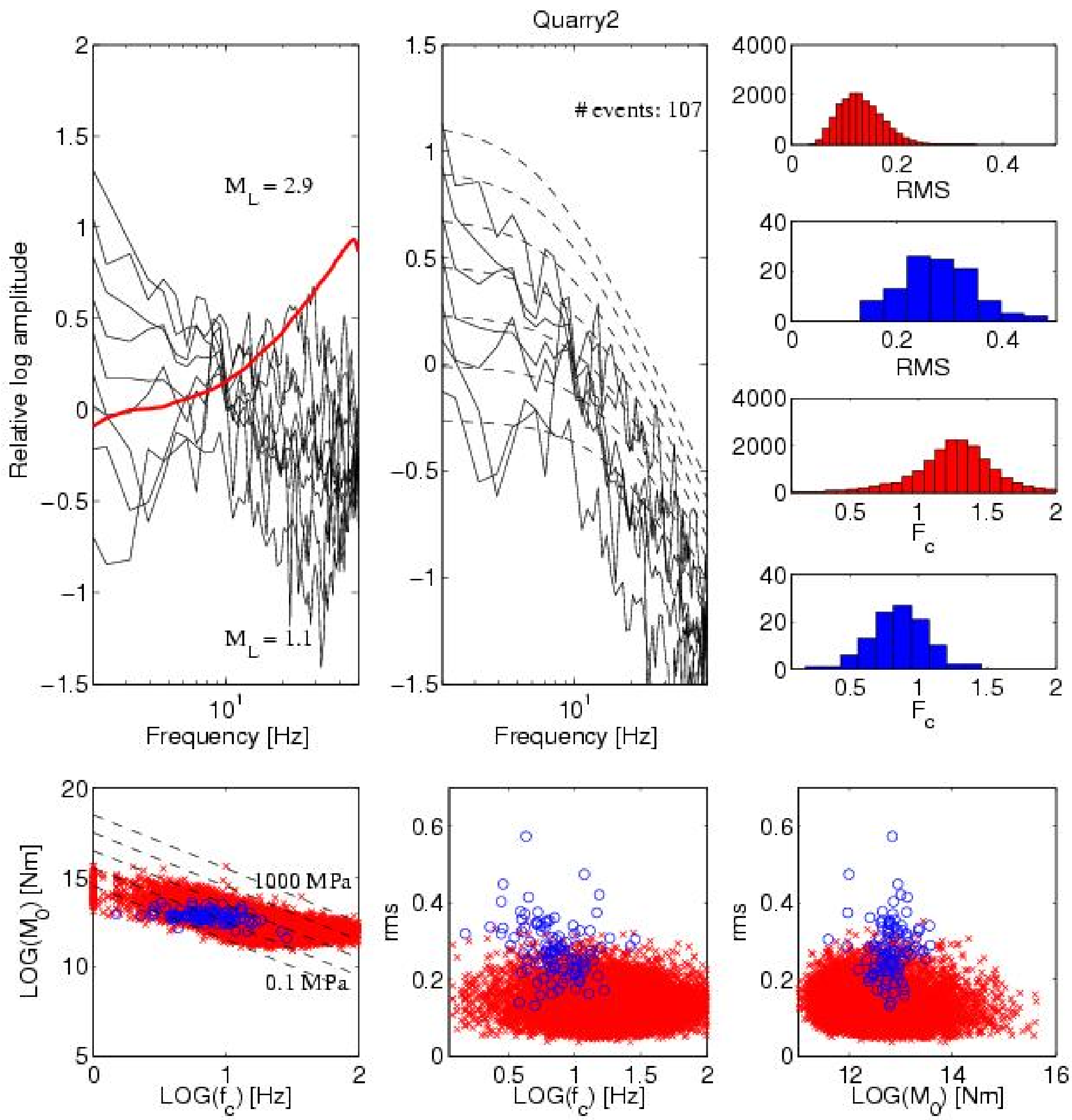

Figure 12. Example quarry 2 (see Fig. 10 for location). Upper left: Stacked quarry blast source spectra in 0.2 local magnitude bins. The red line shows the EGF computed from earthquake spectra. Upper middle: EGF corrected source spectra. Upper right: Histograms of rms-misfit and corner frequency for all earthquakes (red) and the quarry example (blue). The bottom panels from left to right show moment vs. corner frequency, rms-misfit vs. corner frequency, and rms-misfit vs. moment for all earthquakes (red) and the example quarry (blue).

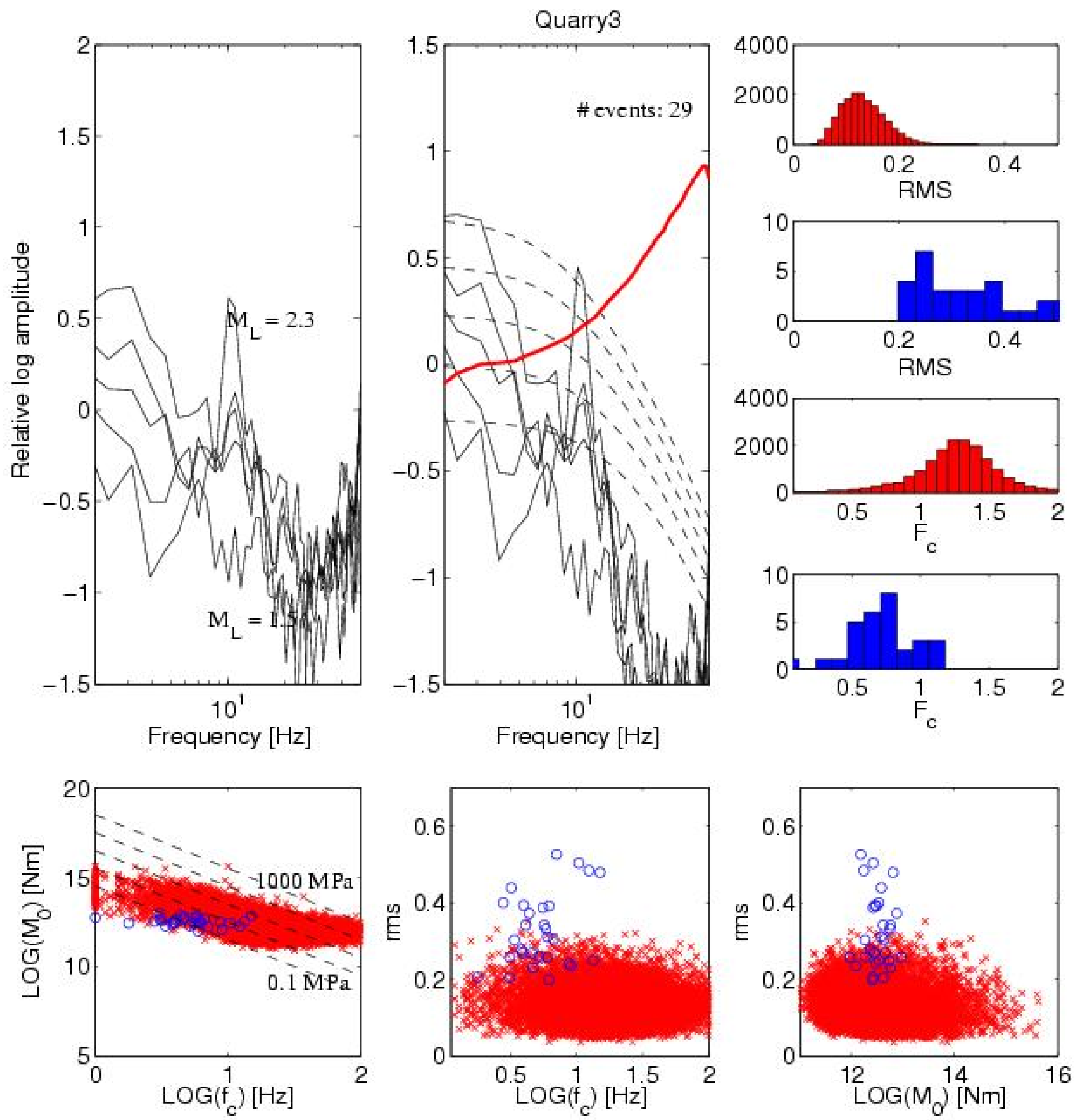

Figure 13. Example quarry 3 (see Fig. 10 for location). Upper left: Stacked quarry blast source spectra in 0.2 local magnitude bins. The red line shows the EGF computed from earthquake spectra. Upper middle: EGF corrected source spectra. Upper right: Histograms of rms-misfit and corner frequency for all earthquakes (red) and the quarry example (blue). The bottom panels from left to right show moment vs. corner frequency, rms-misfit vs. corner frequency, and rms-misfit vs. moment for all earthquakes (red) and the example quarry (blue).

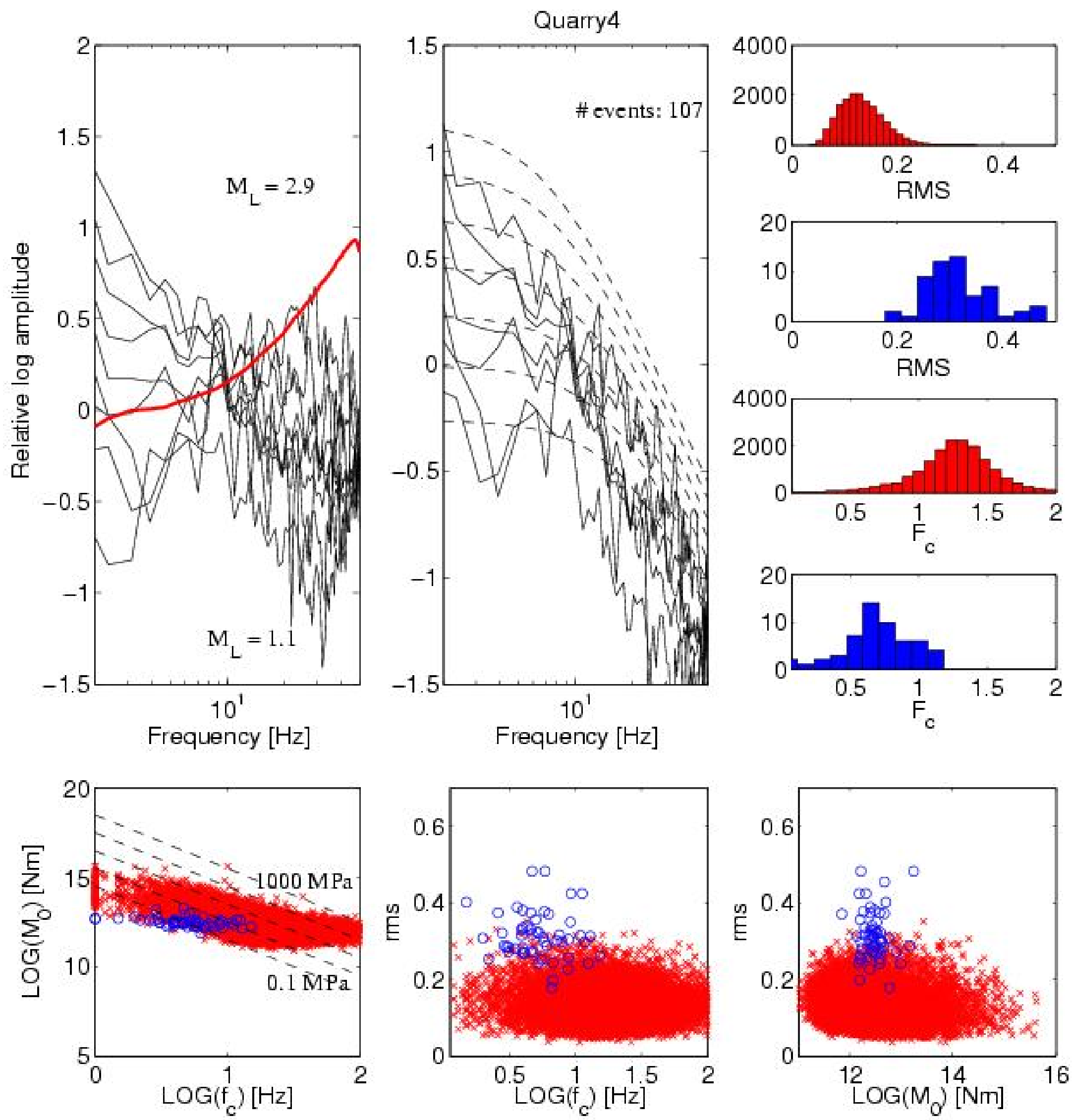

Figure 14. Example quarry 4 (see Fig. 10 for location). Upper left: Stacked quarry blast source spectra in 0.2 local magnitude bins. The red line shows the EGF computed from earthquake spectra. Upper middle: EGF corrected source spectra. Upper right: Histograms of rms-misfit and corner frequency for all earthquakes (red) and the quarry example (blue). The bottom panels from left to right show moment vs. corner frequency, rms-misfit vs. corner frequency, and rms-misfit vs. moment for all earthquakes (red) and the example quarry (blue).

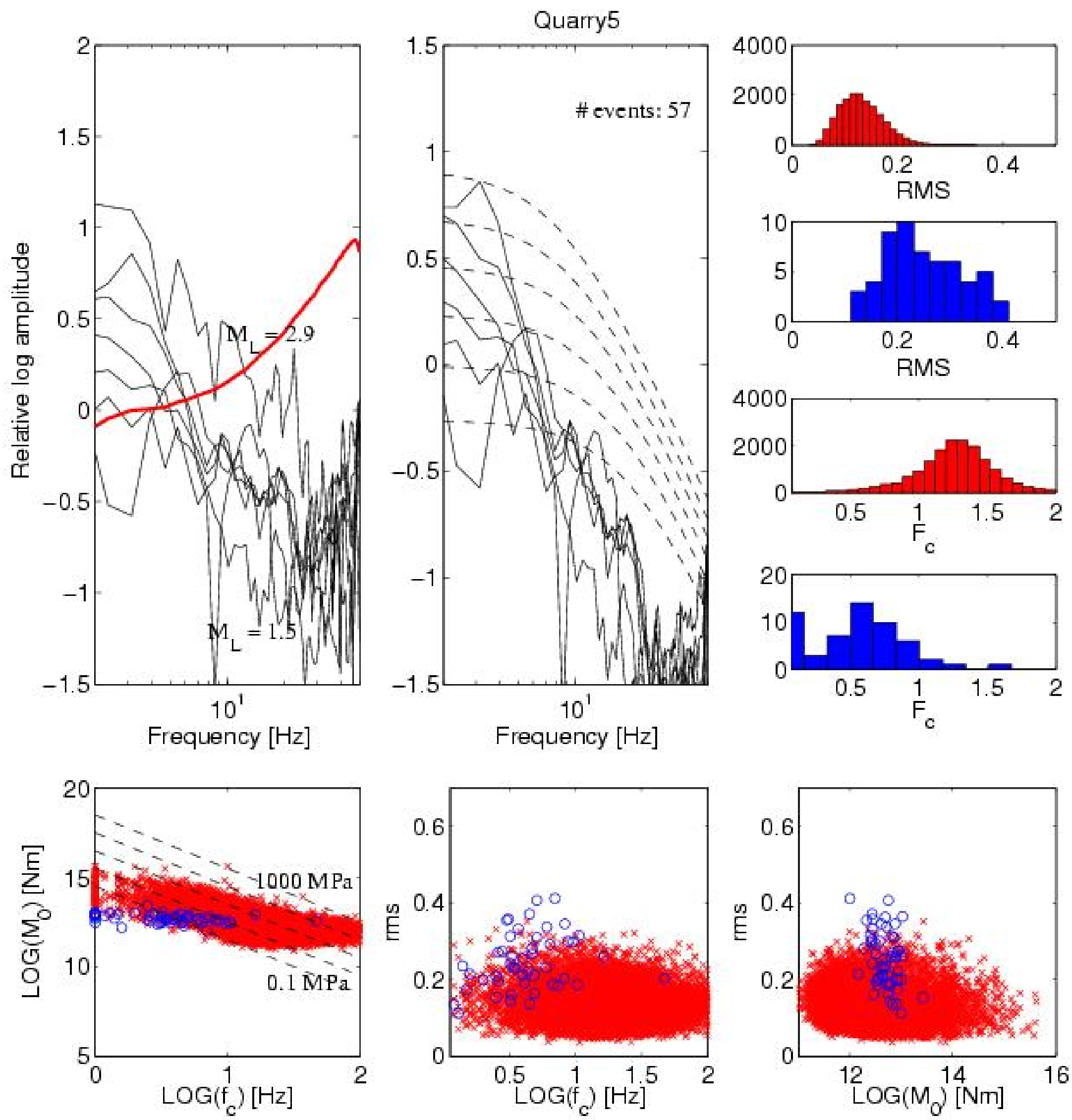

Figure 15. Example quarry 5 (see Fig. 10 for location). Upper left: Stacked quarry blast source spectra in 0.2 local magnitude bins. The red line shows the EGF computed from earthquake spectra. Upper middle: EGF corrected source spectra. Upper right: Histograms of rms-misfit and corner frequency for all earthquakes (red) and the quarry example (blue). The bottom panels from left to right show moment vs. corner frequency, rms-misfit vs. corner frequency, and rms-misfit vs. moment for all earthquakes (red) and the example quarry (blue).

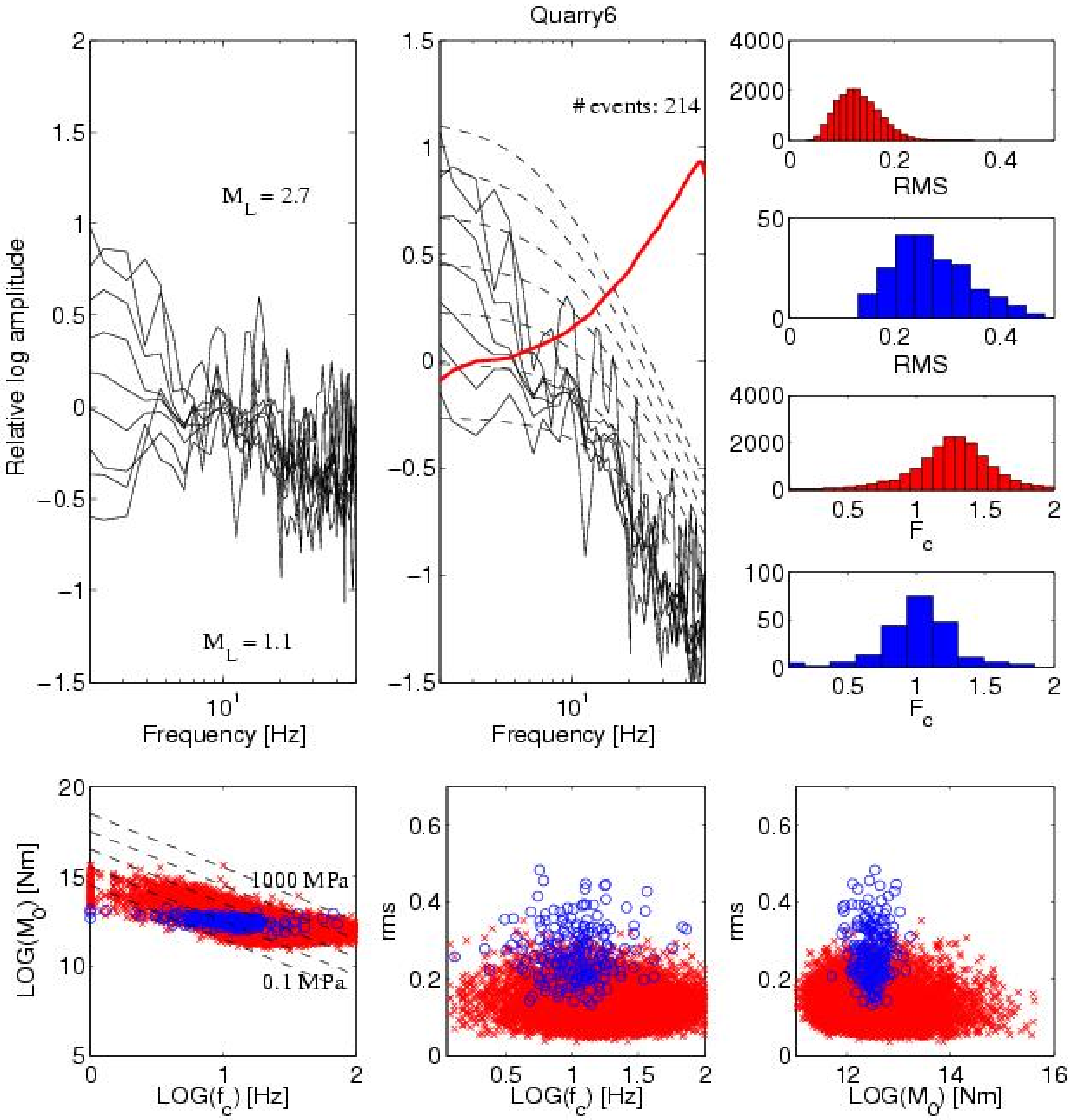

Figure 16. Example quarry 6 (see Fig. 10 for location). Upper left: Stacked quarry blast source spectra in 0.2 local magnitude bins. The red line shows the EGF computed from earthquake spectra. Upper middle: EGF corrected source spectra. Upper right: Histograms of rms-misfit and corner frequency for all earthquakes (red) and the quarry example (blue). The bottom panels from left to right show moment vs. corner frequency, rms-misfit vs. corner frequency, and rms-misfit vs. moment for all earthquakes (red) and the example quarry (blue).

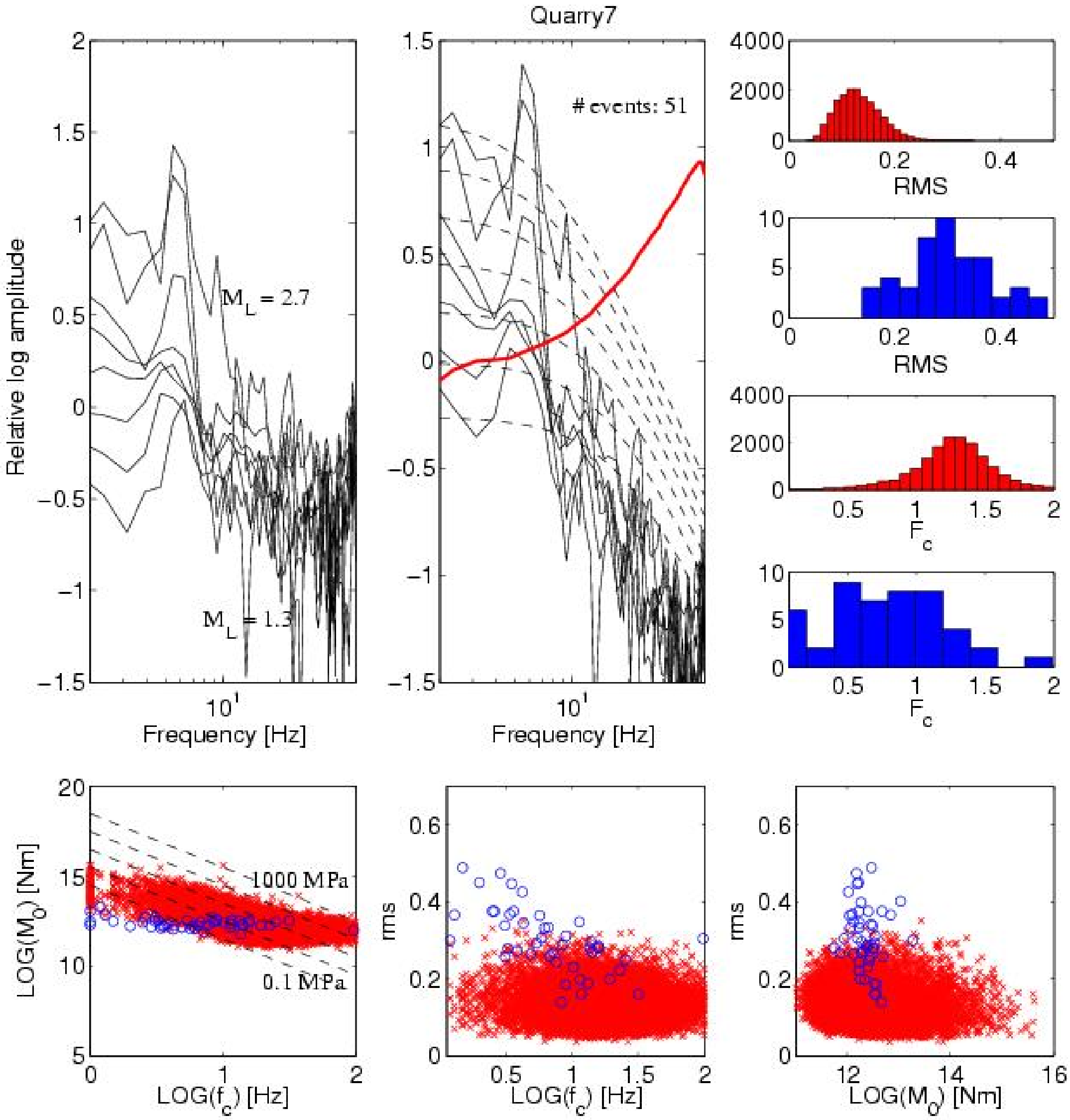

Figure 17. Example quarry 7 (see Fig. 10 for location). Upper left: Stacked quarry blast source spectra in 0.2 local magnitude bins. The red line shows the EGF computed from earthquake spectra. Upper middle: EGF corrected source spectra. Upper right: Histograms of rms-misfit and corner frequency for all earthquakes (red) and the quarry example (blue). The bottom panels from left to right show moment vs. corner frequency, rms-misfit vs. corner frequency, and rms-misfit vs. moment for all earthquakes (red) and the example quarry (blue).

\

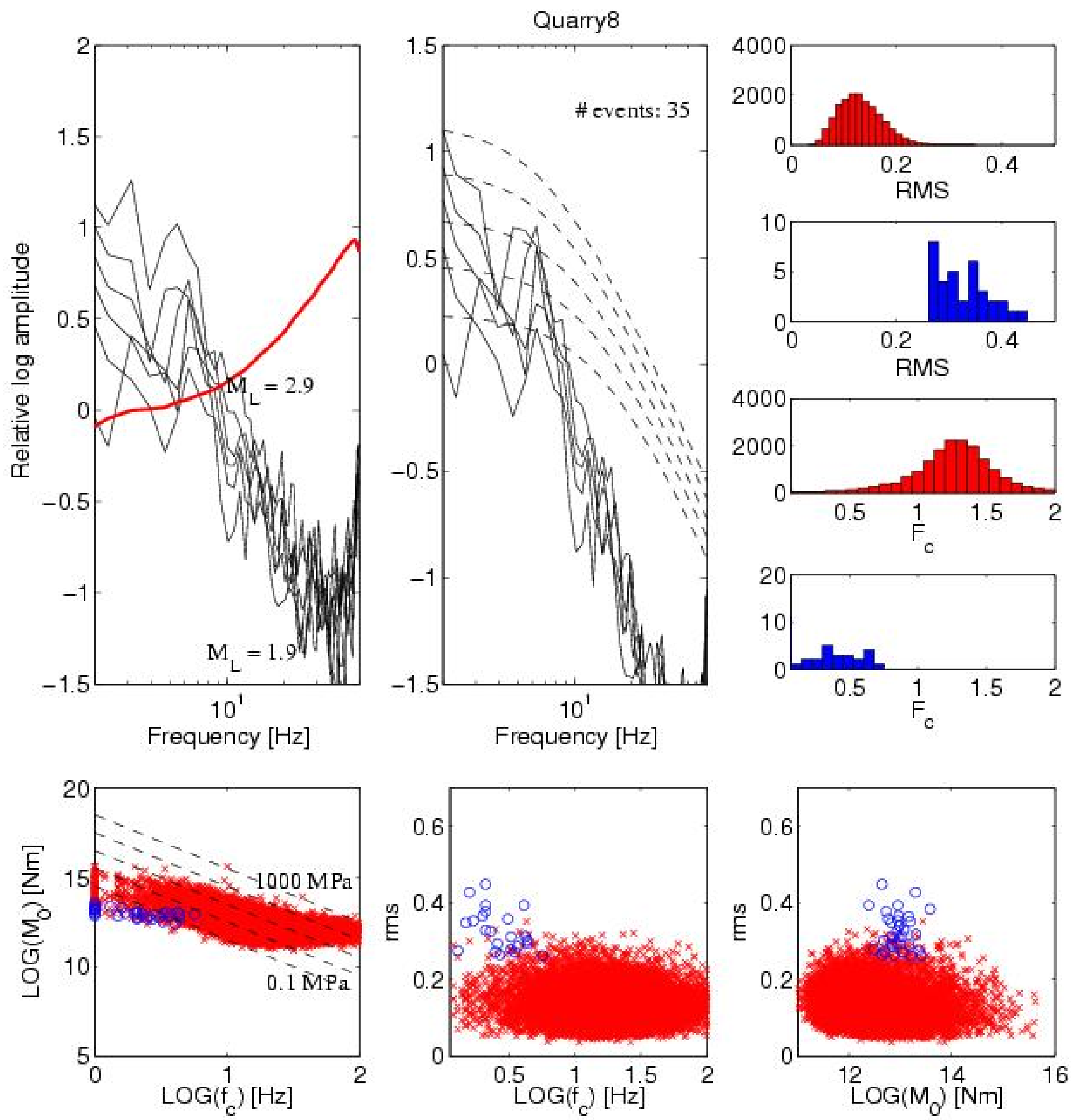

Figure 18. Example quarry 8 (see Fig. 10 for location). Upper left: Stacked quarry blast source spectra in 0.2 local magnitude bins. The red line shows the EGF computed from earthquake spectra. Upper middle: EGF corrected source spectra. Upper right: Histograms of rms-misfit and corner frequency for all earthquakes (red) and the quarry example (blue). The bottom panels from left to right show moment vs. corner frequency, rms-misfit vs. corner frequency, and rms-misfit vs. moment for all earthquakes (red) and the example quarry (blue).

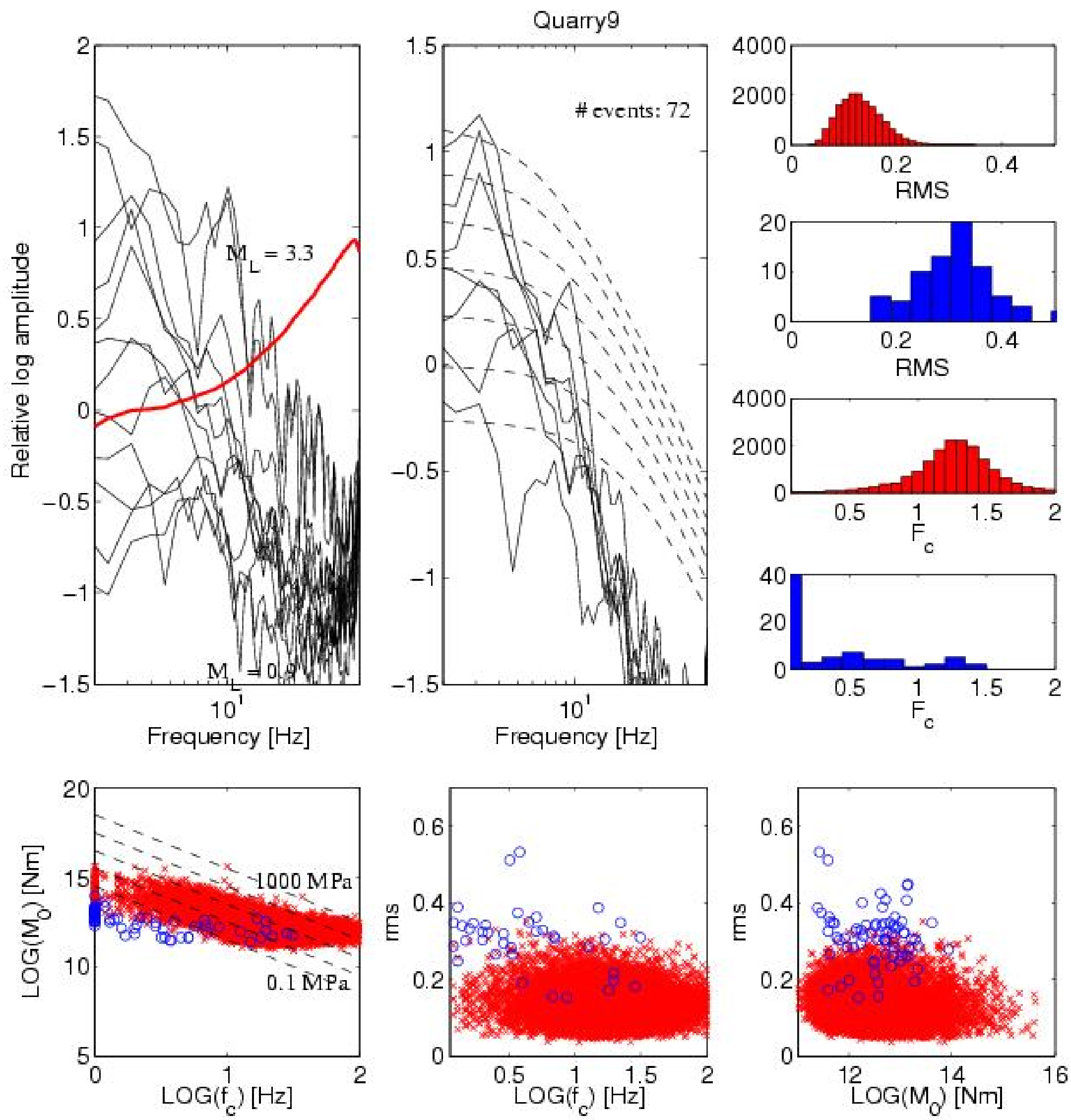

Figure 19. Example quarry 9 (see Fig. 10 for location). Upper left: Stacked quarry blast source spectra in 0.2 local magnitude bins. The red line shows the EGF computed from earthquake spectra. Upper middle: EGF corrected source spectra. Upper right: Histograms of rms-misfit and corner frequency for all earthquakes (red) and the quarry example (blue). The bottom panels from left to right show moment vs. corner frequency, rms-misfit vs. corner frequency, and rms-misfit vs. moment for all earthquakes (red) and the example quarry (blue).

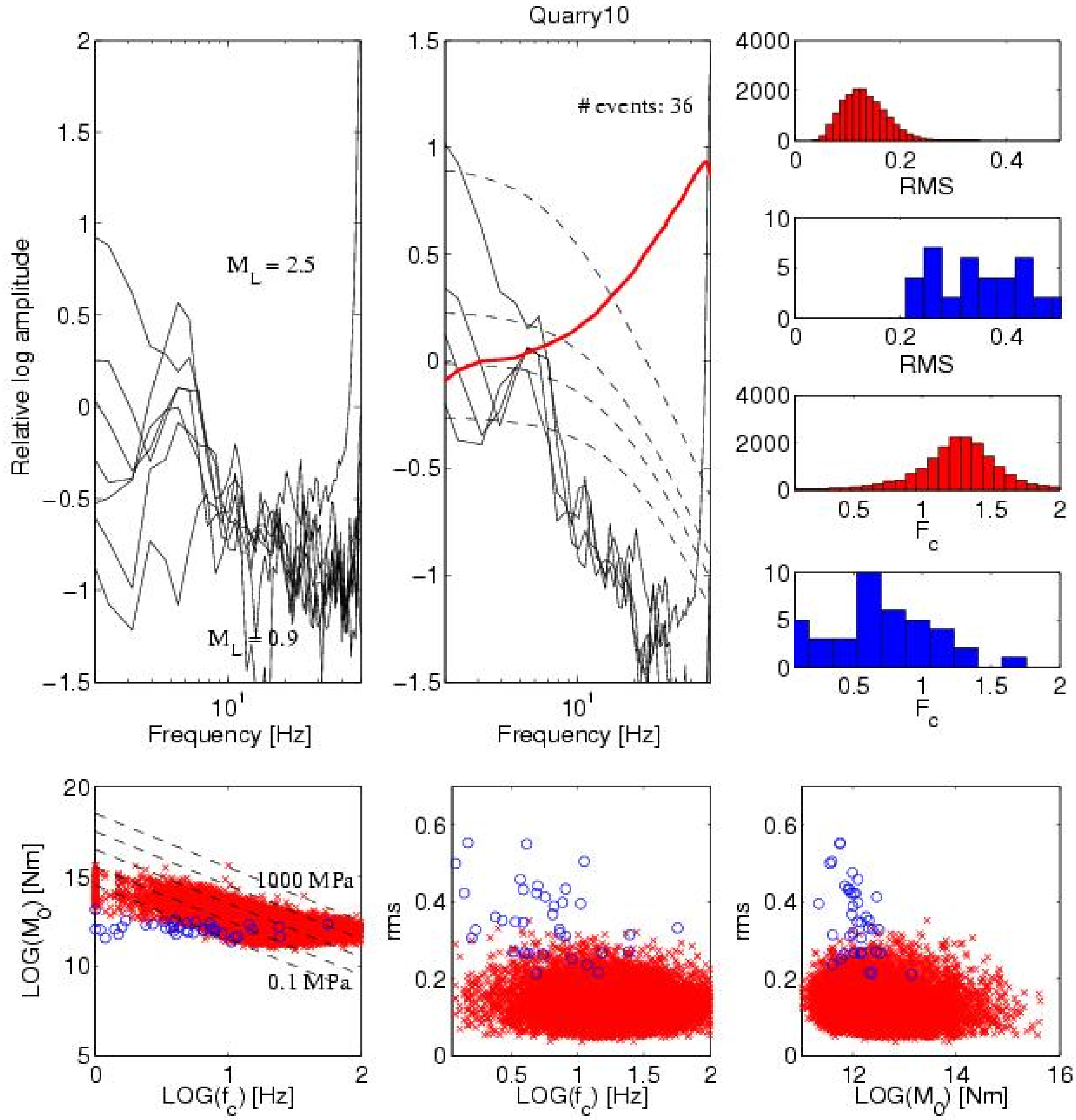

Figure 20. Example quarry 9 (see Fig. 10 for location). Upper left: Stacked quarry blast source spectra in 0.2 local magnitude bins. The red line shows the EGF computed from earthquake spectra. Upper middle: EGF corrected source spectra. Upper right: Histograms of rms-misfit and corner frequency for all earthquakes (red) and the quarry example (blue). The bottom panels from left to right show moment vs. corner frequency, rms-misfit vs. corner frequency, and rms-misfit vs. moment for all earthquakes (red) and the example quarry (blue).

4. CONCLUSIONS

Earthquake and explosions in southern California exhibit significant differences in their average *P*-wave spectral properties. Quarry blast spectra are not well-fit by standard source models and typically have lower corner frequencies and anomalously steep falloffs at high frequencies compared to earthquakes of the same estimated moment. We can therefore establish the RMS misfit between theoretical spectra calculated for a Brune-type source model and the actually observed source spectra as a discriminant between earthquakes and explosions in Southern California. However, we were unable to discriminate unambiguously between earthquakes and explosions. In particular, the two populations still overlap to such an extent that not only an earthquake could be misclassified as an explosions, but also (which is potentially worse) and explosion could remain undetected by being misclassified as an earthquake. On the other hand, we have to assume that the dataset used in this analysis (SCSN catalog) did already include a number of misclassified events, since the flagging of quarry blasts in the SCSN database is based only on event location and the daytime/nighttime distribution. It is in this respect not the ideal dataset to investigate an unambiguous discrimination unless a more rigorous flagging of events can be achieved. Future results from analysis of *S*-wave spectra may provide additional discriminants.

REFERENCES

Arrowsmith, S.J., M.D. Arrowsmith, M.A.H. Hedlin and B. Stump (2006). Discrimination of delay-fired mine blasts in Wyoming using an automatic time-frequency discriminant, *Bull. Seismol. Soc. Am*., **96**, 2368–2382, doi: 10.1785/0120060039.

Bennett, T.J. and J.R. Murphy (1986). Analysis of seismic discrimination capabilities using regional data from western United States events, *Bull. Seismol. Soc. Am*., **76**, 1069–1086.

Carr, D.B. and H.D. Garbin (1998). Discriminating ripple-fired explosions with high-frequency (>16 Hz) data, *Bull. Seismol. Soc. Am*., **88**, 963–972.

Gitterman, Y., V. Pinsky and A. Shapira (1998). Spectral classification methods in monitoring small local events by the Israel seismic network, *J. Seismol*., **2**, 237–256.

Gitterman, Y. and R. van Eck (1993). Spectral of quarry blasts and microearthquakes recorded at local distances in Israel, *Bull. Seismol. Soc. Am*., **83**, 1799–1812.

Hartse, S.E., W.S. Phillips, M.C. Fehler and L.S. House (1995). Single-station spectral discrimination using coda waves, *Bull. Seismol. Soc. Am*., **85**, 1464–1474.

Hauksson, E. and P. Shearer, Southern California hypocenter relocation with waveform cross-correlation, Part 1: Results using the double-difference method, *Bull. Seismol. Soc. Am.*, **95**, 896-903, doi:10.1785/0120040167, 2005.

Hedlin, M.A.H. (1998). A global test of a time-frequency small-event discriminant, *Bull. Seismol. Soc. Am*., **88**, 973–988.

Hedlin, M.A.H., J.-B. Minster and J.A.O. Orcutt (1990). An automatic means to discriminate between earthquakes and quarry blasts, *Bull. Seismol. Soc. Am*., **80**, 2143-2160.

Kim, W.Y., D.W. Simpson and P.G. Richards (1994). High-frequency spectra of regional phases from earthquakes and chemical explosions, *Bull. Seismol. Soc. Am*., **84**, 1365–1386.

Leidig, M.R., B.W. Stump, J.L. Bonner, C.T. Hayward, A.A. Velazco, D.F. Baker, H. Hooper, W.R. Walter, X. Yang, R. Zhou, C.L. Edwards, M.D. Renwald and J.F. Lewkowicz (2004). Source phenomenology experiments in Arizona, *26th Seismic Research Review*, 366–374.

Lin., G., P.M. Shearer and E. Hauksson, Applying a 3D velocity model, waveform cross-correlation, and cluster analysis to locate southern California seismicity from 1981 to 2005, *J. Geophys. Res*., submitted, 2007.

Madariaga, R., Dynamics of an expanding circular fault (1976). *Bull. Seismol. Soc. Am*., **66**, 639–666.

McLaughlin, K.L., J.L. Bonner and R. Barker (2004). Seismic source mechanisms for quarry blasts: modelling observed Rayleigh and Love wave radiation patterns from a Texas quarry, *Geophys. J. Int*., **156**, 79–93.

Musil, M. and A. Plesinger (1996). Discrimination between local microearthquakes and quarry blasts by multi-layer perceptrons and Kohonen maps, *Bull. Seismol. Soc. Am.*, **86**, 1077–1090.

Parolai, S., L. Trojani, M. Frapiccini and G. Monachesi (2002). Seismic source classification by means of a sonogram-correlation approach: Application to data of the RSM Seismic Network (central Italy), *Pure Appl. Geophys.*, **159**, 2763–2788.

Plafcan, D., E. Sandvol, D. Seber, M. Barazangi, A. Ibenbrahim and T.-E. Cherkaoui (1997). Regional discrimination of chemical explosions and earthquakes: a case study in Morocco, *Bull. Seismol. Soc. Am.*, **87**, 1126–1139.

Prieto, G.A., P.M. Shearer, F.L. Vernon and D. Kilb (2004). Earthquake source scaling and self-similarity estimation from stacking P and S spectra, *J. Geophys. Res.*, **109**, doi:10.1029/2004JB003084.

Shearer, P.M., G. Prieto and E. Hauksson (2006). Comprehensive analysis of earthquake source spectra in southern California, *J. Geophys. Res.*, **111**, B06303, doi:10.1029/2005JB003979.

Smith, A.T. (1993). Discrimination of explosions from simultaneous mining blasts, *Bull. Seismol. Soc. Am.*, **83**, 160–179.

Stump, B., M.A.H. Hedlin, D.C. Pearson, and V. Hsu (2002). Characterization of mining explosions at regional distances, *Reviews of Geophysics*, **40(4),** 1011, doi:10.1029/1998RG000048.

Su, F., K. Aki and N.N. Biswas (1991). Discriminating quarry blasts from earthquakes using coda waves, *Bull. Seismol. Soc. Am.*, **81**, 162-178.

Taylor, S.R., N.W. Sherman and M.D. Denny (1988). Spectral discrimination between NTS explosions and western United States earthquakes at regional distances, *Bull. Seismol. Soc. Am.*, **78**, 1563–1579.

Tibuleac, I.M., J. Britton, D.B. Harris, T. Hauk, H. Hooper and J.L. Bonner (2004). Detection methods for mining explosions in southern Asia, *26th Seismic Research Review*, 427–438.

Walter, W. R., K. M. Mayeda, and H. J. Patton (1995). Phase and spectral ratio discrimination between NTS earthquakes and explosions, part I: Empirical observations, *Bull. Seism. Soc. Am.*, **85**, 1050-1067.

Warren, L.M., and P.M. Shearer (2000). Investigating the frequency dependance of mantle Q by stacking P and PP spectra, *J. Geophys. Res.*, **105**, 25,391–25,402.

Warren, L.M., and P.M. Shearer (2002). Mapping lateral variations in upper mantle attenuation by stacking P and PP spectra, *J. Geophys. Res.*, **107**, B12, 2342, doi:10.1029/2001JB001195.

Wuster, J. (1993). Discrimination of chemical explosions and earthquakes in central Europe—a case study, *Bull. Seismol. Soc. Am.*, **83**, 1184–1212.

List of Symbols, Abbreviations, and Acronyms

EGF	Empirical Green's Function
RMS	Root Mean Square
SCSN	Southern California Seismic Network
STN	Signal-To-Noise